Long-time solution of the time-dependent Schrödinger equation for an atom in an electromagnetic field using complex coordinate contours

Liang Tao,[1] W. Vanroose,[2] B. Reps,[2] T. N. Rescigno,[1] and C. W. McCurdy[3,1]

[1]*Chemical Sciences and Ultrafast X-ray Science Laboratory, Lawrence Berkeley National Laboratory, Berkeley, California 94720, USA*
[2]*Wiskunde-Informatica, Universiteit Antwerpen, B-2020 Antwerpen, Belgium*
[3]*Departments of Applied Science and Chemistry, University of California, Davis, California 95616, USA*

We demonstrate that exterior complex scaling (ECS) can be used to impose outgoing wave boundary conditions exactly on solutions of the time-dependent Schrödinger equation for atoms in intense electromagnetic pulses using finite grid methods. The procedure is formally exact when applied in the appropriate gauge and is demonstrated in a calculation of high-harmonic generation in which multiphoton resonances are seen for long pulse durations. However, we also demonstrate that while the application of ECS in this way is formally exact, numerical error can appear for long-time propagations that can only be controlled by extending the finite grid. A mathematical analysis of the origins of that numerical error, illustrated with an analytically solvable model, is also given.

I. INTRODUCTION

In the calculation of electron scattering or photoionization amplitudes using the time-independent Schrödinger equation, physical boundary conditions must be applied to ensure that the scattered solutions contain only outgoing scattered waves. For example, these "purely outgoing" boundary conditions can be expressed for the case of a single electron with energy $\hbar^2 k^2/2m$ in the familiar form $\Psi_{sc} \to f(\theta, \phi) \exp(ikr)/r$ as the radial coordinate of the electron, r, goes to infinity. Applying such boundary conditions to the solution of the Schrödinger equation on a finite grid generally requires matching the solution to the asymptotic form. The idea of complex coordinate scaling is to exploit the analytic properties of the exact solution when viewed along a complex contour in the r plane, and thus replace those explicit boundary conditions with the formally equivalent, but much simpler, condition $\Psi_{sc} \to 0$ along a properly chosen contour.

This idea has been known for decades [1–5], including its generalization to the *exterior complex scaling* (ECS) contour [6,7]. The exterior complex scaling idea, in which the coordinates are made complex only for large values of the coordinates, has recently been exploited with great success in electron impact ionization and double photoionization of atoms and molecules [8–12], where the appropriate boundary conditions are those for two outgoing electrons, and the complex scaling approach is one of the few ways to apply them in a time-independent calculation without approximating the boundary conditions themselves.

The same ideas can be applied to the time-dependent description of photoionization or electron impact ionization, whether involving one or more than one electron [13–15]. However, in the solution of the time-dependent Schrödinger equation, it has also been possible to make use of the easier, albeit approximate, alternative of complex absorbing potentials or masking functions applied near the end of the numerical grid at each time step. Complex absorbing potentials have been applied with particular success for heavy particles

[16–18] and also for electrons where, as Riss and Meyer [19] have carefully analyzed, the longer wavelengths involved complicate the practical application of the idea but not its formal basis. Masking functions [20] have also been used successfully for treating ionization by an intense field.

The application of exterior complex scaling was proposed in the early 1990s [13] as a method for applying outgoing boundary conditions on a finite grid solution of the time-dependent Schrödinger equation and formally avoiding reflections from the edge of the grid. The ECS idea, which we write here for the case of a single electron moving in one dimension for simplicity, is to scale the coordinate of the electron, z, on $(-\infty, +\infty)$ according to the transformation

$$C(z) = \begin{cases} Z_0 + (z - Z_0)e^{i\eta}, & z > Z_0 \\ z, & -Z_0 \le z \le Z_0 \\ -Z_0 + (z + Z_0)e^{i\eta}, & z < -Z_0 \end{cases} \quad (1)$$

as shown in Fig. 1. At the end of the complex domain, in Z_1, homogeneous Dirichlet boundary conditions are enforced. The effect of this transformation on the exact solution of the time-dependent Schrödinger equation for an electron in a field expressed in the velocity gauge is also shown in that figure, and its behavior gives the essence of the application of the ECS idea to particles in a field. When viewed along the complex contour, the wavepacket falls off exponentially with increasing z, and the wave function goes to zero along the contour for any time at which we examine it. Thus, the complex part of the grid need only extend beyond the exterior scaling point, Z_0, a sufficient distance so that the wavepacket is effectively zero at its end. In the region where the coordinates remain real, the wavepacket has the same value as the solution of the unscaled Schrödinger equation, and no approximation has been made except for the discretization error in representing the solution on a grid.

McCurdy *et al.* [13] pointed out that while the application of ECS to the time-dependent Schrödinger equation is completely straightforward and rigorous for potentials that vanish as the interacting particles move apart, the interaction of
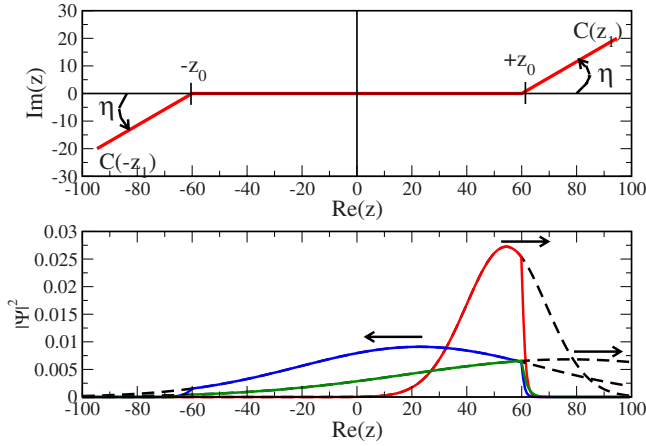
FIG. 1. (Color online) Upper: example exterior complex scaling contour $C(z)$ for one-dimensional problem with z in bohr. Lower: propagation of a Volkov packet with mass of an electron and an initial drift momentum to the right as it oscillates across the ECS boundary at $Z_0 = 60$ bohr. Solid lines: modulus squared of wavepacket (bohr^{-1}) on real portion of contour at three successive times, moving to the right, to the left, and again to the right. Dashed lines: wavepacket on complex portion of contour, plotted for real z.

electrons with electromagnetic fields do not fall into that category. If we represent the interaction of an electron with the electromagnetic field in the length (or so-called electric field) gauge, $V_{int} = e\mathbf{E}(t) \cdot \mathbf{r}$, for a time-varying electric field $\mathbf{E}(t)$, the magnitude of interaction potential increases with the particle's coordinates. Therefore, the application of the ECS transformation leads to pathological behavior of the solutions. On the other hand, those authors pointed out that in the velocity (or radiation) gauge the behavior of the solution of the time-dependent Schrödinger equation is entirely different, and thus the ECS approach can be applied in that gauge instead.

He *et al.* [21] recently revisited this problem and, based on numerical experiments, concluded that the formal arguments of Ref. [13] were incorrect. As a remedy for the numerical instabilities they encountered, they proposed the *ad hoc* procedure of applying ECS only to the kinetic energy operator and leaving all other parts of the Hamiltonian unscaled. We demonstrate here that He *et al.* were mistaken in their conclusions and that the difficulties they encountered were due largely to an inappropriate choice of Z_0, coupled with an ECS grid whose complex portion was prematurely truncated. We also demonstrate that their proposed remedy of scaling only part of the Hamiltonian can produce stable, but physically incorrect results. We show that for any length of propagation for an atom in an ionizing electromagnetic field, it is always possible to pick the ECS contour in Eq. (1), so that the solution vanishes at its ends. The subjects we treat here are important because the advent of ultrafast laser methods, and especially studies of high-harmonic generation by intense short optical pulses, has made it necessary to be able to solve the problem of an atom or molecule in an intense field in a benchmark level calculation without making any approximations that cannot be controlled simply by making the grid representation itself more accurate. A careful analy-

sis of the numerical stability of this approach does show, however, that for any particular contour there is a numerical instability that ultimately appears at long times so that the solution cannot be propagated to arbitrary times. In the absence of an electromagnetic field, no such difficulties appear.

In electromagnetic and acoustic scattering, the ECS contour is known as a *perfectly matched layer* (PML) and was introduced independently by Berenger in 1994 [22]. It has been shown by Chew and Weedon [23] to be equivalent to complex stretching. These methods have found widespread application. However, numerical instabilities have also been observed in simulations with a flow and in anistropic materials. Bécache *et al.* [24] formulated some conditions on the group velocities such that numerical instabilities are avoided.

The outline of the remainder of this paper is as follows. In the following section, we will discuss the behavior of solutions of the time-dependent Schrödinger equation, in the velocity gauge, in the presence of an electromagnetic field in the dipole approximation and describe the model problem that He *et al.* [21] used in their numerical experiments. In Sec. III, we will present the results of numerical calculations that show how the proper choice of the ECS contour eliminates the numerical problems they alleged. In Sec. IV, we will discuss the origins of numerical instabilities for very long integration times. An application to high-harmonic generation will be given in Sec. V, and some concluding remarks will be made in Sec. VI.

II. WAVEPACKETS ON THE ECS CONTOUR

The analytic properties of the time-dependent Schrödinger equation under the ECS transformation can be illustrated with a one-dimensional example, and remain formally the same in three dimensions as well as for more than one particle. In treatments of atoms or molecules in optical fields, the interaction with the electromagnetic field can generally treated in the dipole approximation, and that is the only case we discuss here. We will treat a one-dimensional model of the hydrogen atom, with a soft Coulomb potential, $V_0(z)$. Depending on the gauge chosen for the representation of the field, the time-dependent Schrödinger equation is (atomic units, $m_e = \hbar = e = 1$, will be used throughout)

$$ i\frac{\partial}{\partial t}\Psi(z,t) = \left(-\frac{1}{2}\frac{\partial^2}{\partial z^2} + V_{int}(z,t) + V_0(z)\right)\Psi(z,t). \quad (2) $$

In the electric field (length) gauge, the interaction potential is $V_{int}(z,t) = zE(t)$, where $E(t)$ is the electric field amplitude. In this gauge, it is well-known that the time-independent problem is not dilation analytic [25,26], and the fact that the application of ECS to the time-dependent Schrödinger equation leads to divergent results [13] is therefore no surprise.

In the radiation (velocity) gauge, the situation is quite different, however. In this gauge the momentum operator for an electron in the radiation field becomes $\hat{p}_z + A(t)/c$ and we have

$$V_{\text{int}}(z,t) = -\frac{i}{c}A(t)\frac{\partial}{\partial z} + \frac{A(t)^2}{2c^2}, \tag{3}$$

The soft Coulomb potential used by He *et al.* and that we use here in numerical demonstrations is

$$V_0(z) = -\frac{1}{\sqrt{1+z^2}}. \tag{4}$$

We can understand some of the analytic properties of $\Psi(z,t)$, at least asymptotically, from a semiclassical solution of Eq. (2). Following the procedure of Heller [27], we can write a Gaussian wavepacket corresponding to a locally quadratic approximation to $V_0(z)$ around the central position of the wavepacket, which gives a semiclassical approximation to the exact solution

$$\Psi(z,t) = \exp[i\alpha_t(z-z_t)^2 + ip_t(z-z_t) + i\gamma_t], \tag{5}$$

with the parameters of the packet satisfying the equations of motion

$$\dot{p}_t = -V_0'(z_t) \tag{6}$$

$$\dot{z}_t = p_t + A(t)/c \tag{7}$$

$$\dot{\alpha}_t = -2\alpha_t^2 - V_0''(z_t)/2 \tag{8}$$

$$\dot{\gamma}_t = p_t\dot{z}_t - p_t^2/2 + i\alpha_t - V_0(z_t) - A(t)p_t/c - A(t)^2/(2c^2), \tag{9}$$

where $V_0'(z_t)$ and $V_0''(z_t)$ denote the derivatives of V_0. The solution of these equations depends on the potential of course, and we treat two cases here to explore the analytic properties suggested by the Gaussian approximation and numerically verify those properties for the exact solutions.

A. Analytic properties of $\Psi(z,t)$ for Volkov states

In the case of $V(z,t)=0$ with a vector potential of the simple form $A(t)=A_0\cos(\omega t)$, Eqs. (6)–(9) can be solved exactly and the resulting wavepacket is an exact solution of the time-dependent Schrödinger equation.

$$p_t = p_0 \tag{10}$$

$$z_t = z_0 + p_0 t + \frac{A_0}{\omega c}\sin(\omega t) \tag{11}$$

$$\alpha_t = \frac{\alpha_0}{2\alpha_0 t + 1} \tag{12}$$

$$\gamma_t = \gamma_0 + \frac{p_0^2}{2}t + \frac{i}{2}\ln(2\alpha_0 t + 1) - \frac{A_0^2}{2c^2}\left(\frac{t}{2} + \frac{\sin 2\omega t}{4\omega}\right), \tag{13}$$

where we can choose α_0 to be pure imaginary for simplicity. This wavepacket is a special case of a Volkov packet describing a free electron in a field [28,29].

The analytic properties of this wave function on the contour are determined by the parameters α_t and p_t. McCurdy
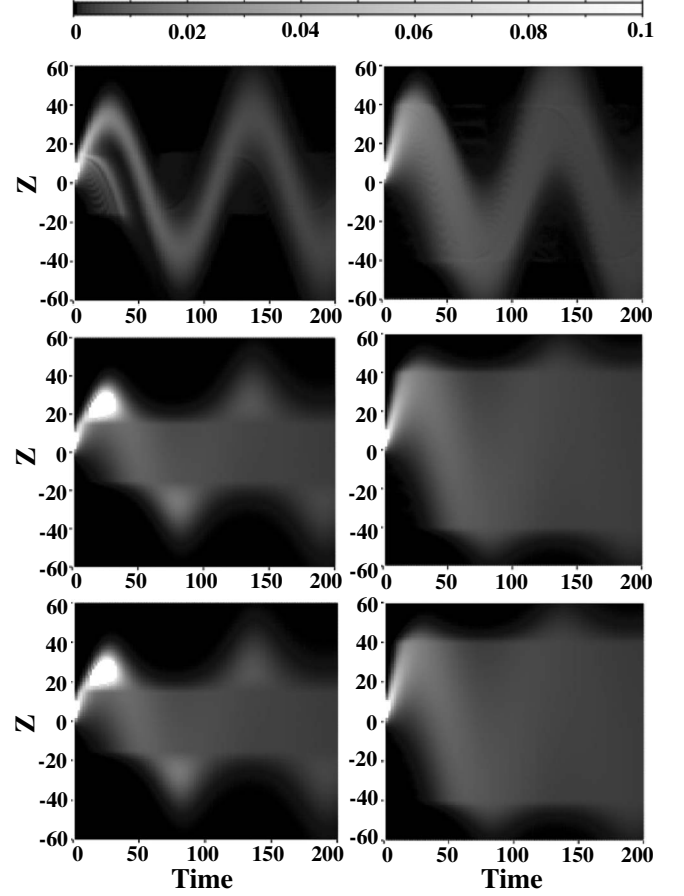

FIG. 2. Modulus squared of Volkov packet on ECS contour as a function of position, z, in bohr and time in atomic time units (24.19×10^{-18} s). Left column: ECS contour with $Z_0=15$, Right column: $Z_0=40$. Top row: results from method of He *et al.* (Ref. [21]). Middle row: correct ECS propagation. Bottom row: analytic solution of time-dependent Schrödinger equation. Quiver radius is 35.1 bohr.

et al. [13] pointed out that when p_t is nonzero, the factor $\exp[ip_t(C(z)-z_t)]$ controls the behavior of the packet on the complex part of the contour as z_t increases past Z_0. As the packet passes Z_0 in the positive z direction, for example, this factor dies off exponentially if $p_t>0$, and that behavior persists for all time because in this gauge, p_t does not change sign (even though z_t is oscillating with the field). This property is exhibited by the Volkov state plotted in Fig. 1. On the other hand, in the electric field (length) gauge p_t oscillates, and as it changes sign, the momentum alternately points inward and outward along the contour, therefore generating locally large values of $\Psi(C(z),t)$ for ranges of z beyond Z_0.

However, in the case that the initial momentum is zero, the quadratic term in the exponent of Eq. (5) solely determines the behavior on the contour. In that case, there are locally large values of $\Psi(C(z),t)$ on the contour if the scaling points $\pm Z_0$ are chosen within the classical quiver radius of the electron, $A_0/\omega c$.

To demonstrate that these analytic properties persist for numerical solutions of Eq. (2) for this case, we have solved the problem using the finite element method in the discrete variable representation (FEM/DVR), and those results for

$|\Psi(C(z),t)|^2$ are shown in Fig. 2. In all cases, the length of the finite elements was either 5 or 10 bohr, the order of the DVR was 15, and the scaling angle, η was 20°. No dependence on the scaling angle is visible on scale of the figures was observed. The distance from $\pm Z_0$ to the end of the ECS contour in each direction was 80 bohr, and at the ends of the grid, the wave function is set to zero by the omission of the last DVR interpolating function from the basis. Crank-Nicolson propagation was used in all the calculations we report here.

The field strength was chosen as $A_0/c = 2$ and $\omega = 0.057$, corresponding to the field of an intense Ti:sapphire laser and a quiver radius of 35.1 bohr. When Z_0 is chosen to be less than half the quiver radius, as it is for the results shown in the left column panels of Fig. 2, locally large values of the wavepacket appear on the complex part of the contour just past Z_0, both in the numerical (middle) and analytical (bottom) calculations, which yield identical results. Simply moving the scaling point, Z_0 out to 40 bohr completely eliminates that behavior, and the numerical and analytical solutions are again identical as shown in the middle and bottom panels of the right column of that figure, but with no large values on the complex part of the ECS contour. Note that in all cases, the values of the numerically propagated wavepacket and the exact solution on the real portion of the grid are identical.

For the numerical implementation of ECS to work properly, it is critical that the complex portion of the grid be chosen long enough to absorb the propagating wavepacket. This is especially critical when Z_0 lies inside the quiver radius. He *et al.* noted, in their low-frequency calculations, an exponential increase in the wavepacket when it entered the complex portion of their grid. They concluded that there was an intrinsic numerical problem with ECS, which they proposed to solve by not analytically continuing the operator describing the interaction with the field, $V_{\text{int}}(z,t)$, onto the exterior scaling contour. In fact, the numerical behavior they observed was a caused by choosing Z_0 smaller than the quiver radius and using too short (12.5 bohr) a complex tail for the grid. In the top row of Fig. 2, we plot results obtained using the modified ECS procedure proposed by He *et al.* and it can be seen that they are quite different from the correct solutions of Eq. (2). The reason for this difference is that by analytically continuing only part of the Hamiltonian, this procedure does not produce an approximation to the analytically continued solution of the original Schrödinger equation. As we will see below, this approach produces similarly spurious results in the presence of a Coulomb potential.

We note in passing that the implementation of ECS in the FEM/DVR and in *B*-splines has been discussed previously in detail [11], and an important point in these numerical implementations is the treatment of the point $z = Z_0$. The sharp changes in slope in Fig. 1 might suggest that numerical errors could result from this behavior. That is not the case, however, because in these implementations, the underlying polynomial basis functions are correctly analytically continued into the complex plane at this point, and the discontinuity in their derivatives is built into these representations analytically [11,30]. Thus, the behavior seen in Fig. 2 when Z_0 is chosen inside the quiver radius for a packet with initial zero momentum has nothing to do with local numerical error and
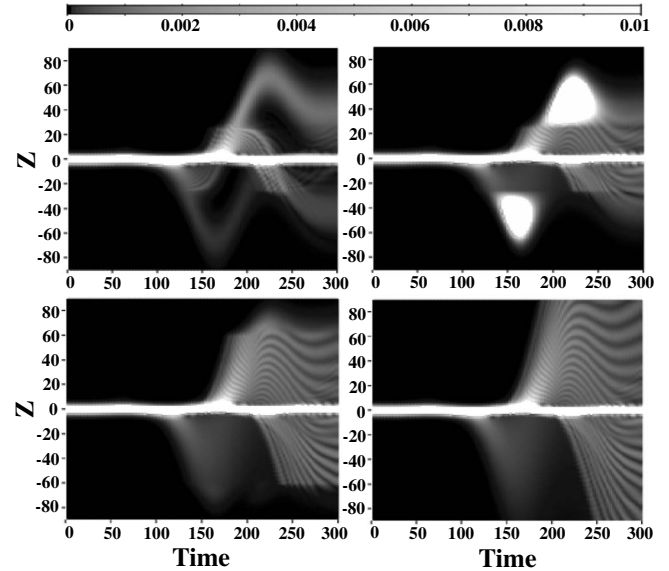

FIG. 3. $|\Psi(C(z),t)|^2$ as a function of time for soft coulomb potential case. Units as in Fig. 2. Top left: results from method of He *et al.* (Ref. [21]) with $Z_0 = 25$ bohr. Top right: correct ECS propagation with $Z_0 = 25$ bohr. Quiver radius is 30.8 bohr. Bottom left: correct ECS propagation with $Z_0 = 60$ bohr. Bottom right: propagation with real grid extending to ± 300 bohr and no complex scaling.

is only a reflection of the analytic properties of the exact solution.

B. Behavior of $\Psi(z,t)$ on the ECS contour for the soft Coulomb potential

In the presence of a Coulomb potential, the solutions of the time-dependent Schrödinger equation on the ECS contour behave in a precisely analogous manner. We can get an indication of the reason by returning to the equations of motion in Eqs. (6)–(9). For the Gaussian approximation to the wavepacket, there are now terms involving $V_0(z)$ and its first and second derivatives at the center of the packet. For short times, before the center of the semiclassical packet has reached sufficiently far from the origin for these terms to be small, the analytic behavior of this approximation to the solution can differ from that discussed above. However, as those terms approach their asymptotic values, the analytic behavior of the approximate solution in the presence of $V_0(z)$ becomes that of the Volkov packet.

In Fig. 3, we demonstrate the solution of the time-dependent Schrödinger equation with the potential of Eq. (4) and compare it with numerical solutions obtained using the procedure of He *et al.* in which only part of the Hamiltonian is continued onto the ECS contour. We use the same parameters appearing in Ref. [21], where the electric field was specified as

$$E(t) = E_0 \sin^2\left(\frac{\pi}{T}t\right)\cos(\omega_0 t), \qquad (14)$$

with $E_0 = 0.1$ and $\omega_0 = 0.057$, and $T = 330$, and therefore we employed the corresponding vector potential $A(t)$ related by

$E(t)=-(1/c)dA(t)/dt$. The corresponding maximum quiver radius is $E_0/\omega^2=30.8$ bohr. The initial wavepacket is the ground state of the field-free Hamiltonian with the potential of Eq. (4), which has an energy of -0.66978 hartrees. We can see that with a value of Z_0 greater than the quiver radius plus the approximate spatial extent of the initial packet, the value of the solution on the ECS contour remains small and becomes exponentially small by the end of the contour.

For all the numerical calculations in Fig. 3, the distance from Z_0 to the end of the ECS contour was 80 bohr. Comparing the top left panel of that figure, which shows results using the method of He *et al.*, with the bottom left panel, which shows ECS propagation with $Z_0=60$, we see notable differences on the real part of the grid. The ECS propagation agrees perfectly with the calculation shown in the bottom right panel using a completely real grid extended to ± 300 bohr to avoid reflections from the ends of the grid.

One has to conclude from these comparisons that the analytic properties of the wave function on the ECS contour are numerically benign, and that the *ad hoc* modification of the Hamiltonian that analytically continues only part of it does not provide a solution to the original problem, although it may resemble it for sufficiently short times.

III. NUMERICAL PROPAGATION TO VERY LONG TIMES ON THE ECS CONTOUR

In the absence of an electromagnetic field, an ionizing solution of the time-dependent Schrödinger equation for an atom or molecule can be propagated, using the methods described above, to arbitrarily long times, essentially until it has vanished from the real part of the grid. In such cases, if the complex portion of the grid, extending from $\pm Z_0$ to the end of the grid in either direction, is made long enough so that the wavepacket does not reach its end with appreciable values, the long-time propagation accumulates discretization error but shows no numerical instabilities. The required length of complex portion of the grid will depend on the momenta involved. However, in the presence of a radiation field, we see a different behavior for long times.

In Fig. 4, we show the results of a numerical experiment for the problems treated in the previous section in Figs. 2 and 3, except that the propagation times are considerably longer. Here, we propagate the Volkov state to $T=500$ and the soft Coulomb wavepacket to 1000 atomic units (for a pulse duration of $T=1100$). The upper panels of Fig. 4 show propagations using small complex portions of the contours, extending 25 and 50 bohr beyond $\pm Z_0$. In those calculations, large peaks appear periodically on both complex sides of the contour, and we see that there is a numerical instability associated with reflections from the end of the ECS contour being amplified by the presence of the field. In the bottom row, the contour extends 75 bohr beyond $\pm Z_0$, which is enough to eliminate the instability for the soft Coulomb example, but it still appears at longer times for the Volkov state with the initial parameters chosen for the Gaussian wavepacket.

Although they can be eliminated by using a longer ECS contour, still much shorter than the real grid necessary to
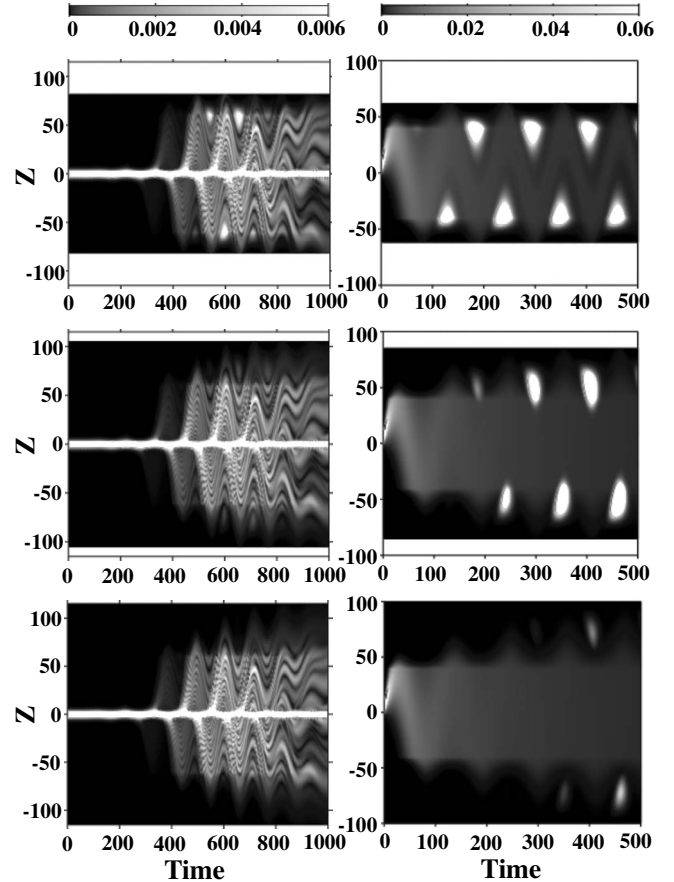

FIG. 4. Long-time propagations. Units as in Fig. 2. Left column: modulus squared of wavepackets from the soft Coulomb potential problem on ECS contour with $Z_0=60$ bohr. Right column: modulus squared of Volkov state wavepackets with $Z_0=40$ bohr. Top row: complex portion of ECS contour is 25 bohr in length. Middle row: complex portion is 50 bohr. Bottom row: complex portion is 75 bohr.

contain the entire wavepacket for such long times, this is nonetheless a qualitatively different behavior than seen in other applications, either time-dependent or time-independent, of the ECS approach. In the next section, we discuss the origins of this behavior.

IV. NUMERICAL ANALYSIS OF ERROR GROWTH DURING LONG-TIME INTEGRATIONS

In this section, we look in detail at the mathematics behind exterior complex scaling. In particular, we look at how enforcing the homogeneous Dirichlet boundary condition at the end of the complex contour ensures that only outgoing waves are allowed at the end of the real part of the grid.

At the same time, we also look at the mathematics that will explain the influence of the ECS contour on the time evolution. Although simulations on the ECS grid in the velocity gauge are long-time stable, we will illustrate that they suffer from short-term error growth. This effect is caused by the fact that the ECS grid turns the Hermitian Hamiltonian into a non-normal operator with particular mathematical properties.

Since the field is switching back and forth over a period T, the dynamics never reach the decaying regime of the uncoupled eigenmodes. It always stays in the regime of short-term exponential growth. This explains the error growth on ECS contours for periodically changing fields. However, the error will have a low spatial frequency with a period equal to the period of the applied field.

A. Bound on the error

During numerical simulation, local rounding and truncation errors are accumulated each time step that affect the final result. We can express the solution of the error equation corresponding to the Schrödinger equation as the sum of two terms

$$\epsilon(t) = e^{-iH(t)}\epsilon(0) + \int_0^t e^{-iH(t-s)}\delta(s)ds, \tag{15}$$

where the first is the propagation of the initial error $\epsilon(0)$, the second term is the local truncation error $\delta(t)$ that is made each time step and propagates over the domain, hence the integral.

An upperbound on the error at time t can be found as

$$\|\epsilon(t)\| \le \|e^{-iH(t)}\|\|\epsilon(0)\| + \max_{0 \le s \le t}\|\delta(s)\| \int_0^t \|e^{-iH(t-s)}\|ds, \tag{16}$$

where $\|\cdot\|$ denotes the L^2 norm. We also take the maximum of the local truncation error over the interval and place it outside the integral. The key to this upperbound is $\|e^{-iH(t)}\|$, the norm of the evolution operator. We use the operator norm that is induced by the vector norm and defined as the supremum of $\|e^{-iH(t)}v\|$ over all possible vectors $v \in V$, a vector space, with $\|v\|=1$. So, to understand this bound on the error, we will analyze the short- and the long-term behavior of $\|e^{-iH(t)}\|$.

B. Non-normal operators

The advantage of the ECS contour is that it absorbs outgoing waves without any reflections, in the exact continuous case, before discretization on a grid or with basis functions. The disadvantage is that it turns the originally Hermitian Hamiltonian into a non-normal operator that alters the short-term behavior of the evolution operator. Indeed, a normal operator A commutes with its Hermitian conjugate, such that $AA^*=A^*A$. We will illustrate, for the continuous (i.e., not discretized) case, that after the ECS transformation, even the simplest differential operator, e.g., $A=d/dz$, is non-normal.

We start by writing the ECS transformation in integral form as in [11],

$$C(z) = \int_0^z q(z)dz. \tag{17}$$

This gives a Jacobian related to the transformation

$$\frac{d}{dC(z)} = \left(\frac{dC(z)}{dz}\right)^{-1}\frac{d}{dz} = \frac{1}{q}\frac{d}{dz}.$$

We then find that

$$AA^* - A^*A = \frac{1}{q}\frac{d}{dz}\frac{1}{q^*}\frac{d}{dz} - \frac{1}{q^*}\frac{d}{dz}\frac{1}{q}\frac{d}{dz} = -\frac{1}{q}\frac{q'^*}{(q^*)^2}\frac{d}{dz} + \frac{1}{qq^*}\frac{d^2}{dz^2}$$
$$+ \frac{1}{q^*}\frac{q'}{q^2}\frac{d}{dz} - \frac{1}{qq^*}\frac{d^2}{dz^2} = \frac{1}{qq^*}\left(\frac{q'}{q} - \frac{q'^*}{q^*}\right)\frac{d}{dz}. \tag{18}$$

This is nonzero for all choices of $q(z)$ that implement exterior complex scaling. In particular, for the ECS transformation

$$q(r) = \begin{cases} 1 & \text{for} \quad r \le R_0 \\ e^{i\theta} & \text{for} \quad r > R_0 \end{cases}, \tag{19}$$

where $q(z)$ has a discontinuous derivative $q'(r) = (e^{i\theta}-1)\delta(r-R_0)$ at R_0, the operator is not normal. In a similar way, it easy to show that the Hamiltonian, which has a second order differential operator, is non-normal after the ECS transformation.

It is known that a non-normal operator may have nonorthogonal eigenvectors [31]. As a consequence, an eigenvalue analysis of the time evolution can only give information about the long-term asymptotic behavior. If the eigenvectors are not orthogonal, the time evolution cannot be uncoupled in the basis of the eigenvectors. Let $c_i(t)=(z_i,u(t))$ be the projection on the i-th eigenstate z_i. Then,

$$i\dot{c}_i(t) = \sum [z_i,H(t)z_j]c_j(t) \ne \lambda_i c_i(t), \tag{20}$$

since $(z_i,z_j) \ne \delta_{i,j}$.

In a similar way, the length of $u(t)$ is not equal to the sum of the projections

$$\|u(t)\|^2 \ne \sum |c_i(t)|^2,$$

which can lead to growth of the total probability.

C. Numerical and spectral abscissa

The time evolution of a system of ordinary differential equations (ODE) with a non-normal time-independent matrix has been studied before [31]. We will introduce the numerical abscissa and spectral abscissa, two mathematical measures that will help us to understand the short-term error growth.

As $t \to \infty$, the asymptotic growth rate of $\|e^{-iHt}\|$, where H is a time-independent Hamiltonian, is determined by

$$\lim_{t \to \infty} t^{-1} \ln\|e^{-iHt}\| = \alpha(-iH), \tag{21}$$

where the spectral abscissa $\alpha(H)$ is defined as

$$\alpha(-iH) = \max_{\lambda_j \in \sigma(H)} \text{Re}(-i\lambda_j).$$

The asymptotic behavior depends on the eigenvalue of $-iH$ with the largest real part. In Fig. 5, we show the eigenvalues with the largest real part for a model with an alternating dc field that we will introduce in the next section.
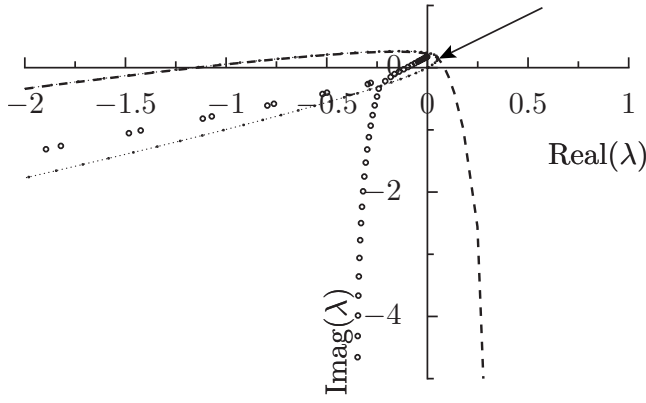
FIG. 5. Spectrum of the time-independent operator of the alternating dc model. Operator is discretized with finite differences on the ECS contour using 100 interior points and 50 points on each of the exterior scaled domains. Spectrum of the operator is shown with circles (○); each mode is stable. The boundary of the numerical range (dashed line) significantly protrudes into the region with positive real parts, resulting in short-term growth. Dotted line: the boundary of the numerical range generated by the complex part of the ECS contour only. The rightmost point, indicated with the arrow, is the numerical abscissa of this subset of $\mathbb{C}$ and gives an estimate for the error growth discussed in Sec. IV E.

On the other hand, the short-term behavior, as $t \to 0$, is determined by the numerical range, defined as the set of complex values reached by the Rayleigh quotient, x^*Ax/x^*x, of vectors with length one. If $H_n \in \mathbb{C}^{n \times n}$ is a numerical representation of H, we then have the definition of the numerical range

$$W(-iH_n) = \{-ix^*H_nx \in \mathbb{C}: \|x\|_2 = 1, x \in \mathbb{C}^n\}. \quad (22)$$

In Fig. 5, we show, for the same model, the numerical range. In contrast to the eigenvalues, the numerical range significantly protrudes into part of the complex plane with positive real part.

The short-term behavior is determined by

$$\lim_{t \to 0} t^{-1} \ln\|e^{-iH_nt}\| = \omega(-iH_n), \quad (23)$$

where $\omega(-iH_n)$ is the numerical abscissa. It is the largest real part of complex points in $\mathbb{C}$ that lie inside the numerical range $W(-iH_n)$. Only normal operators have the same numerical and spectral abscissa, and the short- and long-term behavior is the same.

In our problem, however, after the introduction of the ECS transformation and the representation of the Hamiltonian on a grid, the operator is non-normal and the spectral and numerical abscissa differ significantly. This is also clear from Fig. 5. In particular, the spectral abscissa has a *negative* real part that ensures a decaying long-term behavior. In contrast, the numerical abscissa has a *positive* real part that leads to a short-term growth. Fig. 6 shows the difference in short-term growth and long-term decay for a model problem we present in the next section.
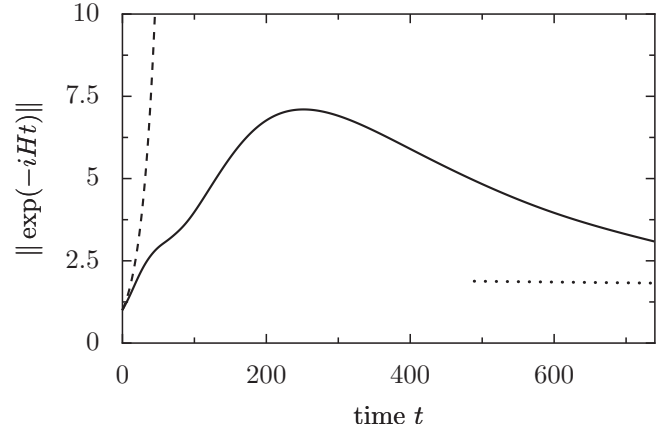

FIG. 6. Time evolution of the norm of the exponential operator for the model problem with $a_0 = 0.6$ discretized on a finite difference grid and an ECS angle of 30°, with time in atomic units $(24.19 \times 10^{-18}$ s). Since the operator is non-normal the numerical and spectral abscissa differ. The spectral abscissa is negative while the numerical abscissa is positive, leading to a short-term growth, but there is long-term decay. Dashed line shows the initial growth while the dotted line is the asymptotic decay rate given by the eigenvalue with the largest real part. Note that at $t=0$, the norm of $\|\exp(-iHt)\| = 1$.

D. Error analysis for an analytically solvable problem

1. Model with vector potential that is piecewise constant in time

In order to understand the behavior of the error at the boundaries, we present a minimal model. It has an alternating vector potential that is constant in one direction during the first half a period T and constant in the other direction for the remainder of the period. When the initial state is a wavepacket, an exact analytical expression gives the position and shape of the wavepacket at all times. The equation is

$$i\frac{\partial u(z,t)}{\partial t} = \left(-\frac{1}{2}\frac{\partial^2}{\partial z^2} - \frac{i}{c}A(t)\frac{\partial}{\partial z} + \frac{1}{2c^2}A(t)^2\right)u(z,t), \quad (24)$$

with

$$A(t) = \begin{cases} +a_0c & \text{if } nT \le t < (n+1/2)T \\ -a_0c & \text{if } (n+1/2)T \le t < (n+1)T \end{cases} \quad \forall \, n \in \mathbb{N}. \quad (25)$$

Again, this model problem can be solved exactly, if the state at the beginning of a half period is described by a Gaussian wavepacket

$$\Psi(z,t) = \exp[i\alpha_0(z-z_0)^2 + ip_0(z-z_0) + i\gamma_0]. \quad (26)$$

During that half period, the parameters evolve as

$$z(t) = z_0 + p_0t - a_0t,$$

$$p(t) = p_0,$$

$$\alpha(t) = \alpha_0/(2\alpha_0t + 1),$$

$$\gamma(t) = \gamma_0 + p_0^2 t/2 + i \ln(2\alpha_0 t + 1)/2 - a_0^2 t/4. \quad (27)$$

These equations also determine the shape of the wavepacket at the end of a period given the parameters at the start of a period. By applying these equations recursively, it is possible to get an analytical expression for the shape of the solution at any time.

Since the Hamiltonian is time-independent over intervals of duration $T/2$, an eigenvector, eigenvalue and numerical range analysis of the time evolution can give us more insight into the behavior of the error at the boundaries.

2. Eigenmode analysis of model problem

Since the operator of the model problem is constant during half a period, an analysis based eigenvalues and the numerical range is possible. The Hamiltonian for a constant vector potential is

$$H = -\frac{1}{2}\frac{\partial^2}{\partial C(z)^2} - ia_0\frac{\partial}{\partial C(z)} + \frac{1}{2}a_0^2, \quad (28)$$

where a_0 is positive for this discussion. The results for $-a_0$ are the same, with the sign reversed. We denote u_j for eigenstate and λ_j the corresponding eigenvalue.

It can be shown [32] that for a finite difference, discretization with a sufficiently large number of grid points, all the eigenvalues lead to stable modes.

For this discussion, we consider the left-hand side of the domain. The same analysis is valid on the other side of the domain. In the complex domain, beyond the point of exterior scaling, Z_0, the equation is a second order ODE with constant coefficients and the solution can be written, $\forall z \geq Z_0$, as a linear combination of two fundamental solutions

$$u_j(z) = A \exp[i(-a_0 + \sqrt{2\lambda_j})C(z)]$$
$$+ B \exp[i(-a_0 - \sqrt{2\lambda_j})C(z)]. \quad (29)$$

Now at the end of the domain, at $C(Z_1)$, homogeneous Dirichlet boundary conditions $u[C(Z_1)] = 0$ are enforced. It follows that the ratio of the coefficients is

$$\frac{|B|}{|A|} = \exp(-2\{\text{Re}(\sqrt{2\lambda_j})\text{Im}[C(Z_1)] + \text{Im}(\sqrt{2\lambda_j})\text{Re}[C(Z_1)]\}). \quad (30)$$

We conclude that the effect of the ECS rotation is that B, the coefficient of the incoming wave, is suppressed exponentially with respect to the outgoing wave. This holds for each of the eigenmodes, as long as the λ_j is such that

$$\text{Re}(\sqrt{2\lambda_j})\text{Im}[C(Z_1)] + \text{Im}(\sqrt{2\lambda_j})\text{Re}[C(Z_1)] > 0. \quad (31)$$

Note that not each eigenmode is suppressed in the same way. Eigenmodes with $|\lambda_j| \gg 1$ are better suppressed than eigenmodes with small $|\lambda_j|$. The suppression, however, is independent of the field strength a_0.

In the presence of a field, it is not necessary that the full solution is exponentially decaying in the absorbing boundary. Indeed, in the presence of the field the fundamental solutions can be *both* incoming or outgoing. If $|\lambda_j|$ is very small, it might be that both $-a_0 + \sqrt{2\lambda_j}$ and $-a_0 - \sqrt{2\lambda_j}$ have the same
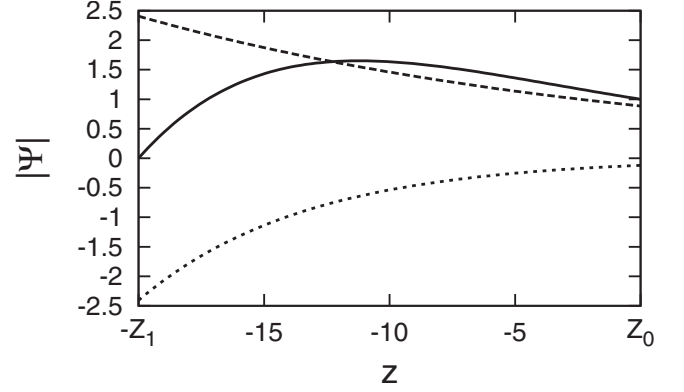

FIG. 7. For the eigenmodes for the model problem with constant vector potential of Sec. IV D 1 with $|\lambda_j| \ll a_0$, the wave functions, Ψ, as functions of z (in bohr) for both the fundamental modes (broken curves), are exponentially increasing on the left complex contour. The Dirichlet boundary condition forces the sum of the two to be zero at $-Z_1$. The sum of the two, shown as the solid line, is increasing in the initial part of the complex contour and then bends over to fit the homogeneous Dirichlet boundary condition at $z = -Z_1$.

sign in Eq. (29). So situations can appear where enforcing the Dirichlet boundary conditions suppresses one of the two incoming waves but leaves the other incoming wave unattenuated. The overall wave function will then grow at the onset of the complex rotation. In a way, this is the correct physical picture. The electrons that move faster than the field should be suppressed. The waves that are slower should not be suppressed since they will return to the target as the field is reversed.

We give an example. Let $a_0 = 0.2$ and take an ECS contour with $\theta = \pi/6$ and length $L = 20$. Let the eigenmode have $\sqrt{2\lambda_j} = 0.1$. On the ECS contour, the eigenstate is written as a linear combination $A \exp(i0.3e^{i\theta}z) + B \exp(i0.1e^{i\theta}z)$. Enforcing the Dirichlet boundary condition at $Z_1 = -20$ then gives $|B| = |A|\exp[-0.2 \text{ Im } C(Z_1)]$. The total wave function is still exponentially increasing on the left complex contour as shown in Fig. 7.

E. Estimate of the short-term error growth

In this section, we estimate the short-term growth. As discussed earlier, this is determined by the numerical abscissa $\omega(-iH_n)$, which is the real part of the rightmost point in the numerical range $W(-iH_n)$. To estimate this short-term growth, we will look for the rightmost point in a subset of the numerical range.

Let H_n be a finite difference semidiscretization of Eq. (24), i.e., the numerical representation of the operator on the ECS grid, where we approximate the spatial differential operator with the help of central differences as

$$\frac{d^2u(x)}{dx^2}\bigg|_{x=x_i} = \frac{u(x_{i+1}) - 2u(x_i) + u(x_{i-1})}{h^2} + \mathcal{O}(h^2)$$

$$\left.\frac{du(x)}{dx}\right|_{x=x_i} = \frac{u(x_{i+1}) - u(x_{i-1})}{2h} + \mathcal{O}(h^2). \qquad (32)$$

The Rayleigh quotients of a vector $v \in \mathbb{C}^n$ with $v_k = [\exp(i\varphi)]^k$ for all $\varphi \in [0, 2\pi]$ gives the symbol curve that encloses a subset of the numerical range. The definition and properties of symbol curves are discussed in [31]. Furthermore, we have found that the rightmost points of the numerical range come from the complex part of the ECS grid [32]. We therefore look at the symbol of the tridiagonal submatrix $\widetilde{H}_n$ of H_n representing the complex ECS contour. This is a diagonally constant matrix

$$(\widetilde{H}_n v)_j = \frac{e^{-2i\theta}}{2h^2}(-e^{i(j+1)\varphi} + 2e^{ij\varphi} - e^{i(j-1)\varphi})$$
$$- ia_0 \frac{e^{-i\theta}}{2h}(e^{i(j+1)\varphi} - e^{i(j-1)\varphi}) + \frac{1}{2}a_0^2 e^{ij\varphi}, \qquad (33)$$

where $e^{-i2\theta}$ comes from the complex rotation of the grid on the contour with an angle θ.

$$\Rightarrow \frac{v^* \widetilde{H}_n v}{v^* v} = \frac{\sum_j v_j^* H_n v_j}{\sum_j v_j^* v_j}$$
$$= \frac{e^{-2i\theta}}{h^2}[-\cos(\varphi) + 1] - a_0 \frac{e^{-i\theta}}{h}\sin(\varphi) + \frac{1}{2}a_0^2.$$

The imaginary part of $\frac{v^* \widetilde{H}_n v}{v^* v}$,

$$-\sin(2\theta)[-\cos(\varphi) + 1]/h^2 + a_0 \sin(\theta)\sin(\varphi)/h,$$

is the real part of $v^*(-i\widetilde{H}_n)v/v^* v$. The extremum $\varphi_{\max} \in [0, 2\pi]$ satisfies

$$\tan(\varphi_{\max}) = ha_0 \frac{\sin(\theta)}{\sin(2\theta)}, \qquad (34)$$

where $0 < \varphi_{\max} \leq \pi$ corresponds to the maximum. The extreme point is then

$$\alpha(-i\widetilde{H}_n) = -a_0 \frac{\sin(\theta)}{h}\frac{\cos(\varphi_{\max}) - 1}{\sin(\varphi_{\max})}, \qquad (35)$$

which is positive since $0 < \sin(\varphi_{\max})$. For weak fields a_0, we can approximate

$$\frac{\cos(\varphi_{\max}) - 1}{\sin(\varphi_{\max})} = \frac{1 - \sqrt{1 + \tan^2(\varphi_{\max})}}{\tan(\varphi_{\max})} \approx -\frac{1}{2}\tan(\varphi_{\max}).$$
$$(36)$$

We then get an estimate for the numerical range

$$\alpha(-i\widetilde{H}_n) \approx \frac{1}{2}\frac{\sin^2(\theta)}{\sin(2\theta)}a_0^2. \qquad (37)$$

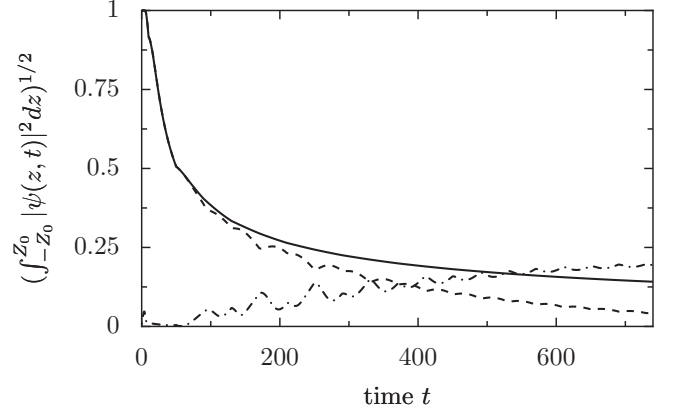Since $\widetilde{H}_n$ is a submatrix of H_n, the numerical ranges are subsets. Therefore,

FIG. 8. Time evolution of total probability on interior of the domain for model problem with alternating dc field with time in atomic units (24.19×10^{-18} s). Solid line: exact solution based on Eq. (26); dashed line: numerical solution; dashed-dot line: error in the total probability. At time $t = 400$, i.e., five periods, the error exceeds the numerical solution. Note that the error is mainly low frequency. The period is $T = 80$, $a_0 = 0.6$, $L = [-13, 13]$; we used 100 grid points on the interior of the domain. Each complex contour has a length 13 and has 50 grid points. Crank-Nicholson is used for the numerical time integration.

$$\alpha(-i\widetilde{H}_n) \leq \alpha(-iH_n). \qquad (38)$$

We have used Eq. (38) to estimate the initial growth in Fig. 6. We have also indicated the extreme point in Fig. 5.

F. Error growth in a periodic field

In a periodic problem, where the field changes periodically over time, there is always a short-term growth when the field changes. If the period is comparable to the timescale of this short-term growth, the numerical simulation never reaches the long-term decaying behavior determined by the eigenvalues. This leads to a continuously growing error. This is illustrated in Fig. 8, where we compare, for the exactly solvable model of equation (24), the total probability on the real part of the domain. The total probability of the exact problem decays because the packet propagates onto the complex portion of the contour. The numerical simulation also decays, but because of the short-term error growth, there is a continuously growing error. As time increases, the numerical and the exact solution start to deviate significantly from each other.

This error is in the low energy components of the wave packet. Indeed, as shown in Fig. 5, the modes on the complex contour that protrude into the right half of the complex have a small momentum. This explains why the numerical experiments show an error with a low spatial frequency.

V. HIGH-HARMONIC GENERATION WITH PROPAGATION ON THE ECS CONTOUR

Once understood, the numerical instabilities discussed above can be avoided in practice for any maximum propagation by an appropriate choice of the ECS contour. As a dem-

onstration of the practical utility of the ECS approach to the solution of the time-dependent Schrödinger equation for atoms and molecules in an electromagnetic field, we calculate the high harmonics generated by the one-dimensional soft Coulomb model treated in Sec. II B. The formulation we use to extract the spectral density function from a given wavepacket propagation follows that used by Telnov and Chu [33,34], who treated high-harmonic generation (HHG) using the Floquet method combined with complex scaling in prolate spheroidal coordinates. In that work, Telnov and Chu found a multiphoton resonance phenomenon in the HHG spectrum, and we find the same phenomenon in this model, provided long enough pulses are employed.

Again, we make use of a sine squared pulse shape so that the vector field is specified by a central photon frequency ω_0, a duration, T, and a field strength A_0

$$A(t) = A_0 \sin^2\left(\frac{\pi}{T}t\right)\sin(\omega_0 t). \qquad (39)$$

We will use field intensities between 10^{12} and 10^{14} W/cm^2, and pulse durations of 60 cycles of the central frequency $\omega_0 = 0.057$, corresponding to $T = 160$ fs, so in the absence of complex scaling the wavepacket would extend over a broad range of z, much larger than the ECS contour, by the end of the pulse.

The harmonic spectrum can be calculated from the Fourier transform, $\tilde{D}(\omega)$, of the time-dependent dipole moment, $D(t)$,

$$D(t) \equiv \langle \Psi_t | z | \Psi_t \rangle$$

$$\tilde{D}(\omega) = \frac{1}{T} \int_0^T e^{i\omega t} D(t) dt \qquad (40)$$

in terms of which we can express the spectral density of the radiation energy $S(\omega)$ emitted over the duration of the pulse [34],

$$S(\omega) = \frac{2\omega^4}{3\pi c^3} |\tilde{D}(\omega)|^2. \qquad (41)$$

In finite grid solutions of the time-dependent Schrödinger equation, it is more convenient to relate $S(\omega)$ to the Fourier transform of an operator that is more localized on the atom so that it can be calculated accurately without large grids, and the ECS method is no exception. We require a quantity whose representation converges on $(-Z_0, Z_0)$. Thus, we calculate the dipole acceleration

$$a(t) = \frac{d^2}{dt^2} D(t), \qquad (42)$$

which, using Ehrenfest's theorem, and the Hamiltonian in the form $H = \frac{1}{2}[\hat{p}_z + A(t)/c]^2 + V_0(z)$, can be shown to satisfy [33]
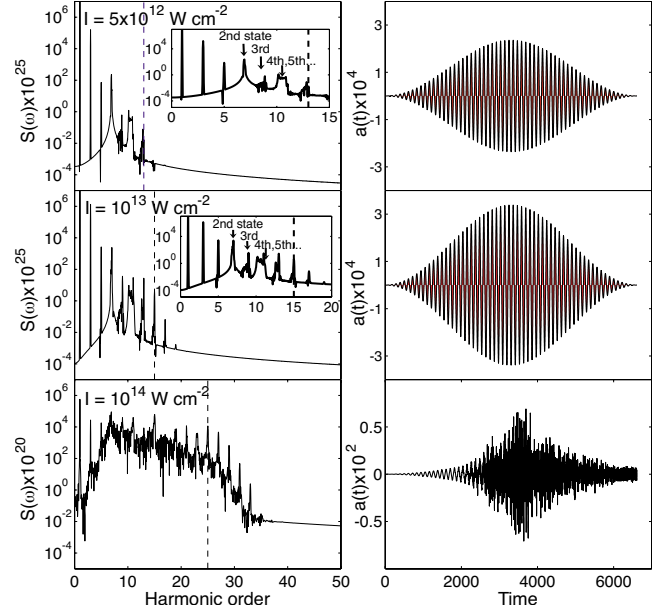

FIG. 9. (Color online) Left column: spectral energy density in atomic units (hartrees × atomic time unit) for harmonic generation in the soft Coulomb potential problem, with 60 cycle pulse and intensities varying (top to bottom) 5×10^{12}, 10^{13}, and 10^{14} W/cm^2. Dashed vertical line: classical cutoff at $(I_p + 3.17U_p)/\omega_0$. Right column: corresponding dipole acceleration, with time in atomic units (24.19×10^{-18} s).

$$a(t) = -\frac{\langle \Psi(z,t)| \frac{d}{dz} V_0(z) |\Psi(z,t)\rangle}{\langle \Psi(z,t)|\Psi(z,t)\rangle} - E(t), \qquad (43)$$

where $E(t)$ is the electric field amplitude corresponding to Eq. (40). In these calculations, the integrals in Eq. (44) were taken only over the real part of the ECS contour. Defining the Fourier transform of $a(t)$ as in Eq. (41), and making use of the relation $\tilde{a}(\omega) \approx \omega^4 |\tilde{D}(\omega)|^2$ [33], we calculate the spectral density of the harmonics as

TABLE I. Energies (in hartrees) of the eigenstates of the soft Coulomb potential of Eq. (4) and the approximate harmonic order to which the transition energies correspond.

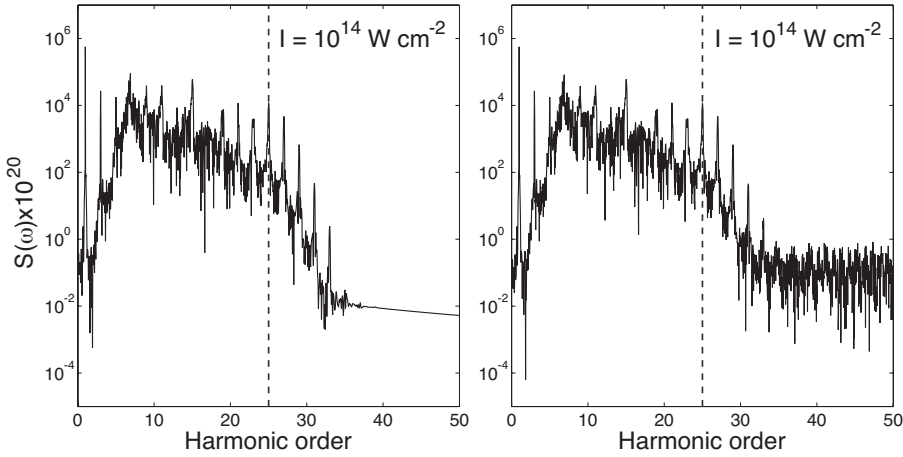| Eigenstate n	E_n	$(E_n - E_1)/\omega_0$
1	−0.66978	0
2	−0.27489	6.93
3	−0.15145	9.09
4	−0.09268	10.13
5	−0.06353	10.64
6	−0.04547	10.95
7	−0.03425	11.15
8	−0.02471	11.32
9	−0.01499	11.49
10	−0.00283	11.70

FIG. 10. Harmonic generation. Left: $S(\omega)$ from ECS calculation using a 60 cycle pulse with central frequency $\omega_0=0.057$ atomic units and intensity of 10^{14} W/cm^2. Right: calculation using same pulse parameters using method of Ref. [21]. Units as in Fig. 9

$$S(\omega) = \frac{2}{3\pi c^3}|\tilde{a}(\omega)|^2. \qquad (44)$$

In Fig. 9, we show the spectral densities of harmonics generated by the 160 fs pulse in Eq. (40) for intensities of 5×10^{12}, 10^{13}, and 10^{14} W/cm^2 together with the corresponding dipole accelerations, $a(t)$. The ECS contour has $Z_0=70$ bohr, and the complex part of grid is chosen to extend an additional 100 bohr. The time step for the Crank-Nicolson propagation of the wave function was $\Delta t=0.02$.

Although for shorter pulses, these harmonic spectra vary considerably with pulse duration, for pulses longer than sixty cycles, they do not change appreciably. The dipole acceleration can be seen to change qualitatively as the intensity reaches 10^{14} W/cm^2. The harmonic spectra are consistent with the classical cutoff number [35], $N=(I_p+3.17U_p)/\omega_0$, where the ionization potential, I_p is given by the energy of the ground state in Table I, and the ponderomotive potential is given by $U_p=I/(4\omega_0^2)$. Those cutoff numbers for the intensities 5×10^{12}, 10^{13}, and 10^{14} W/cm^2 are shown by dashed lines at $N=13$, 15, and 25, respectively.

In their calculations on HHG from H_2^+, Telnov and Chu found resonance features in $S(\omega)$ when the transition energies from the ground to bound excited states of the target molecule correspond to the frequencies of particular harmonic orders. The intensities of those harmonics are strongly enhanced by these resonances. For the soft Coulomb potential treated here, we can see from Table I that the transition between the first and second states corresponds almost exactly to the frequency of the seventh harmonic, and that the transition to the third eigenstate almost perfectly matches the ninth harmonic. The insets in Fig. 9 show strong enhancements of those harmonics for intensities of 5×10^{12} and 10^{13} W/cm^2. Transitions to the fifth and higher states of the Rydberg series can be seen to intensify and change the peak shapes of the 11th and 13th harmonics. Long pulses are required to see these effects in $S(\omega)$ clearly.

Finally, in Fig. 10, we show a comparison of the ECS results at the highest intensity we consider here with a calculation on the same grid using the procedure of He *et al.* [21], to demonstrate which parts of the harmonic spectral density are modified by the spurious components of the wave function generated by not properly analytically continuing

the solution onto the ECS contour. In that figure, one sees that in this case, it is primarily the cutoff region that is adversely affected.

VI. CONCLUSION

In this paper, we have analyzed the application of the ECS method to the dynamics of electrons in intense laser fields, and concluded that the pathological numerical behavior that He *et al.* [21] observed in the application of this idea in the radiation gauge was an artifact of the grid parameters they chose. Moreover, the formal arguments used in Ref. [21] to explain that behavior are evidently in error. We have demonstrated numerically that a choice of the ECS contour that places the exterior scaling radius Z_0 inside the region covered by the spatial extent of the initial packet plus the quiver radius leads to perfectly understandable and completely avoidable apparent numerical pathologies. To further emphasize those points, we have presented another numerical demonstration, requiring converged, long-time integrations, of the calculation of high harmonics using the ECS method.

Nonetheless, a careful mathematical analysis shows that, for long times, the error in numerical propagation of the solution of the time-dependent Schrödinger equation using the ECS contour has a surprising behavior. Because the Hamiltonian under ECS is non-Hermitian and therefore is a non-normal operator, and because of the boundary conditions forcing the solution to zero at the ends of the grid, a significant difference can appear between the short- and long-term behaviors of the error during time integration.

We have examined the mathematics that explains this contrasting behavior and analyzed these two time scales for one-dimensional models of the dynamics of electrons in intense laser fields. In the radiation (velocity) gauge, the simulations are long-term stable. On the other hand, there can be significant short-term error growth that scales with the square of the strength of the electric field.

In periodic problems, the dynamics never reaches the regime of long-term decay of the error. Since the field is changing, it always stays in the regime with short-term growth. This means that the error can grow significantly during the simulations. We have found, however, that the calculation of the high-harmonic spectrum is hardly affected by

this error in practice, in part because the error affects low energy components of the solution and evolves on a different timescale from the high harmonics.

An aim of the numerical analysis we present here is to find conditions on the numerical grid, ECS boundary, and applied fields, such that we can estimate and therefore control, *a priori*, the numerical error in ECS calculations on atoms and molecules in fields. Such estimates will allow large-scale and high-dimensional calculations to be carried out on systems with two active electrons and moving nuclear degrees of freedom without empirical exploration of the numerical parameters of the simulation.

[1] E. Balslev and J. M. Combes, Commun. Math. Phys. **22**, 280 (1971).
[2] J. Aguilar and J. M. Combes, Commun. Math. Phys. **22**, 269 (1971).
[3] W. Reinhardt, Annu. Rev. Phys. Chem. **33**, 223 (1982).
[4] B. Simon, Commun. Math. Phys. **27**, 1 (1972).
[5] Y. K. Ho, Phys. Rep. **99**, 1 (1983).
[6] C. A. Nicolaides and D. R. Beck, Phys. Lett. A **65**, 11 (1978).
[7] B. Simon, Phys. Lett. A **71**, 211 (1979).
[8] T. N. Rescigno, M. Baertschy, W. A. Isaacs, and C. W. McCurdy, Science **286**, 2474 (1999).
[9] W. Vanroose, F. Martín, T. N. Rescigno, and C. W. McCurdy, Science **310**, 1787 (2005).
[10] W. Vanroose, D. A. Horner, F. Martín, T. N. Rescigno, and C. W. McCurdy, Phys. Rev. A **74**, 052702 (2006).
[11] C. W. McCurdy, M. Baertschy, and T. N. Rescigno, J. Phys. B **37**, R137 (2004).
[12] D. A. Horner, C. W. McCurdy, and T. N. Rescigno, Phys. Rev. A **78**, 043416 (2008).
[13] C. W. McCurdy, C. K. Stroud, and M. K. Wisinski, Phys. Rev. A **43**, 5980 (1991).
[14] C. W. McCurdy, D. A. Horner, and T. N. Rescigno, Phys. Rev. A **65**, 042714 (2002).
[15] D. A. Horner, C. W. McCurdy, and T. N. Rescigno, Phys. Rev. A **71**, 012701 (2005).
[16] R. Kosloff and D. Kosloff, J. Comput. Phys. **63**, 363 (1986).
[17] J. G. Muga, J. P. Palao, B. Navarro, and I. L. Equsquiza, Phys. Rep. **395**, 357 (2004).
[18] T. Gonzalez-Lezana, E. J. Rackham, and D. E. Manolopoulos, J. Chem. Phys. **120**, 2247 (2004).
[19] U. V. Riss and H.-D. Meyer, J. Phys. B **26**, 4503 (1993).
[20] J. L. Krause, K. J. Schafer, and K. C. Kulander, Phys. Rev. A **45**, 4998 (1992).
[21] F. He, C. Ruiz, and A. Becker, Phys. Rev. A **75**, 053407 (2007).
[22] J.-P. Berenger, J. Comput. Phys. **114**, 185 (1994).
[23] W. C. Chew and W. H. Weedon, Microwave Opt. Technol. Lett. **7**, 599 (1994).
[24] E. Bécache, S. Fauqueux, and P. Joly, J. Comput. Phys. **188**, 399 (2003).
[25] C. Cerjan, R. Hedges, C. Holt, W. P. Reinhardt, K. Scheibner, and J. J. Wendoloski, Int. J. Quantum Chem. **14**, 393 (1978).
[26] J. E. Avron and I. W. Herbst, Commun. Math. Phys. **52**, 239 (1977).
[27] E. J. Heller, J. Chem. Phys. **62**, 1544 (1975).
[28] H. R. Reiss, Phys. Rev. A **22**, 1786 (1980).
[29] L. A. Collins and A. L. Merts, Phys. Rev. A **37**, 2415 (1988).
[30] C. W. McCurdy and F. Martín, J. Phys. B **37**, 917 (2004).
[31] L. N. Trefethen and M. Embree, *Spectra and Pseudospectra: The Behavior of Nonnormal Matrices and Operators* (Princeton University Press, Princeton, NJ, 2005).
[32] B. Reps and W. Vanroose (unpublished).
[33] D. A. Telnov and Shih-I Chu, Phys. Rev. A **71**, 013408 (2005).
[34] D. A. Telnov and Shih-I Chu, Phys. Rev. A **76**, 043412 (2007).
[35] P. B. Corkum, Phys. Rev. Lett. **71**, 1994 (1993).